Sonotherapy Using Folic Acid-Ag-Bi_2O_3 Nanocomposites in 2D and 3D Cultural C540 Melanoma Cells

Mina Sarani (PhD Candidate)[1], Paria Tamaddon (MSc)[2], Hanieh Haghighi (MSc)[1], Hossein Heli (PhD)[1], Majid Darroudi (PhD)[3], Arash Safari (PhD)[4], Mohammad Reza Sardashti Birjandi (PhD)[5], Gholamhossein Tondro (PhD)[6,7], Zahra Kayani (PhD)[8], Naghmeh Sattarahmady (PhD)[1,2]*

[1] Nanomedicine and Nanobiology Research Center, Shiraz University of Medical Sciences, Shiraz, Iran
[2] Department of Medical Physics and Engineering, School of Medicine, Shiraz University of Medical Sciences, Shiraz, Iran
[3] Nuclear Medicine Research Center, Mashhad University of Medical Sciences, Mashhad, Iran
[4] Department of Radiology, School of Paramedical Science, Shiraz University of Medical Sciences, Shiraz, Iran
[5] Department of Chemical Engineering, University of Sistan and Baluchestan, 98164-161, Zahedan, Iran
[6] Infectious Disease Research Center, Aja University of Medical Sciences, Tehran, Iran
[7] Department of Microbiology, Faculty of Medicine, Aja University of Medical Sciences, Tehran, Iran
[8] Barriers in Inflammation Laboratory, VIB Center for Inflammation Research, Ghent, Belgium

*Corresponding author: Naghmeh Sattarahmady
Nanomedicine and Nanobiology Research Center, Shiraz University of Medical Sciences, Shiraz, Iran
E-mail: nsattar@sums.ac.ir

Received: 18 May 2025
Accepted: 21 July 2025

ABSTRACT

Background: Sonodynamic Therapy (SDT) is increasingly recognized as an innovative, non-invasive cancer modality in which low-intensity Ultrasound (U) energizes sonosensitizers, provoking a burst of Reactive Oxygen Species (ROS) that culminate in apoptotic destruction of tumor cells.

Objective: Silver-bismuth oxide nanocomposites (AgB NCs) and their folic acid-functionalized counterparts (FAgB NCs) studied as sono-sensitizers for improving in treatment route of melanoma cancer.

Material and Methods: In this experimental research, AgB NCs and FAgB NCs were synthesized via a green route using *Rheum turkestanicum* extract. Comprehensive physicochemical characterizations-including Field-Emission Scanning Electron Microscopy (FESEM), Energy-Dispersive X-ray spectroscopy (EDX), Ultraviolet visible spectrometer (UV-vis), Powder X-ray Diffraction (PXRD), and Fourier-Transform Infrared spectroscopy (FT-IR)-confirmed the successful formation and functionalization of the nanocomposites.

Results: (3-(4, 5-dimethylthiazolyl-2)-2, 5-diphenyltetrazolium bromide) (MTT) assays on C540 melanoma cells revealed dose-dependent cytotoxicity, with F-AgBi NCs exhibiting significantly lower IC_{50} values compared to AgB NCs. Upon U exposure, nanocomposites induced substantial ROS generation, mitochondrial dysfunction, and increased apoptosis, as verified by flow cytometry. Moreover, the FAgB NCs effectively suppressed cell migration and inhibited spheroid formation in 3D cultures, indicating potent antitumor activity in both monolayer and 3D models.

Conclusion: These findings underscore the synergistic potential of folic acid-functionalized AgB nanocomposites as efficient sonosensitizers for targeted melanoma therapy. Their enhanced ROS-mediated cytotoxicity, combined with folate receptor-targeted delivery, supports their application in advanced nanomedicine and SDT-based cancer treatment.

Keywords

Sonodynamic Therapy; Reactive Oxygen Species; Folic Acid; Ag-Bi_2O_3 Nanocomposites; Nanomedicine; Ultrasound-Mediated Apoptosis

Introduction

Melanoma represents a highly aggressive and metastatic form of cancer that necessitates the development of advanced therapeutic approaches for successful intervention [1-3]. This malignancy originates from the unchecked growth of melanocytes located in the basal layer of the epidermis and is driven by various contributing factors, including prolonged Ultraviolet (UV) radiation exposure, genetic alterations, and immune system disturbances [4,5]. The Tumor Microenvironment (TME) significantly influences melanoma advancement by fostering intercellular signaling, enhancing oxidative stress, and facilitating metastasis, particularly under UV stimulation [6,7]. Due to its invasive characteristics and resistance to standard treatment methods, there is a critical demand for more targeted and effective therapeutic alternatives.

Sonodynamic Therapy (SDT) is a novel, non-invasive approach for cancer treatment that leverages low-frequency Ultrasound (U) to activate specific sonosensitizing agents, resulting in the generation of Reactive Oxygen Species (ROS) that promote apoptosis in malignant cells [8-11]. This technique offers notable benefits such as the ability to penetrate deep into tissues, reduced systemic toxicity, and precise targeting of tumor regions. The ROS produced during SDT interfere with mitochondrial integrity, cause DNA fragmentation, and initiate apoptotic signaling cascades including Mitochondrial Permeability Transition Pore (MPTP) formation and calcium ion imbalance [12-16]. The therapeutic success of SDT is closely linked to the characteristics of the sonosensitizer-especially its ROS-generating efficiency, tumor specificity, and biocompatibility [8-11].

ROS in SDT is primarily produced through sonoluminescence and pyrolysis. Sonoluminescence results from the collapse of cavitation bubbles, emitting photons that initiate radical (type I) or singlet oxygen (type II) reactions [17,18]. Pyrolysis involves the decomposition of water molecules by U-induced heat, generating hydroxyl and hydrogen radicals [19,20]. Additionally, U-induced hyperthermia further sensitizes tumor cells to ROS-mediated damage [21,22]. Despite its promise, the clinical application of SDT has been limited by the drawbacks of conventional organic sonosensitizers, including poor stability, rapid clearance, and limited tumor accumulation [23-25].

Recent advances in nanotechnology have introduced engineered nanomaterials as next-generation sonosensitizers, offering improved tumor targeting, increased ROS production, and enhanced biological stability [26]. Among these, bismuth oxide (Bi_2O_3)-based nanocomposites have attracted attention due to their high atomic number (Z=83), potent radiosensitizing properties, and strong X-ray attenuation, making them ideal for theranostic applications [27-31]. Silver nanoparticles (Ag NPs), known for their potent cytotoxic and antimicrobial effects, further enhance the therapeutic potential of such nanostructures [32-36]. Combining Ag and Bi_2O_3 in a single nanoplatform can synergistically boost SDT performance through elevated ROS production and improved cancer cell targeting [26,28,32].

To improve targeting specificity, nanoparticles are frequently modified with folic acid because of its strong binding affinity to folate receptors, which are abundantly expressed in several cancer types, including melanoma [37,38]. This functionalization promotes receptor-mediated endocytosis, thereby enhancing cellular internalization and minimizing unintended interactions with non-cancerous tissues.

In the present investigation, silver-bismuth oxide nanocomposites (AgB NCs) were synthesized through an eco-friendly approach employing *Rheum turkestanicum* extract as a natural reducing and stabilizing agent. Subsequent surface functionalization with folic acid yielded folate-conjugated nanocomposites (FAgB NCs). Comprehensive physicochemical analyses were conducted to validate the structural integrity and functional attributes of the synthesized nanomaterials. Furthermore, their therapeutic performance was systematically evaluated in both two-dimensional (2D) monolayer and three-dimensional (3D) spheroid cultures of melanoma cells. The results highlight the synergistic enhancement of ROS-mediated cytotoxicity and apoptosis arising from the dual action of folic acid-mediated targeting and U-induced activation. Collectively, these findings contribute to the advancement of a selective, biocompatible nanoplatform with significant potential for application SDT of malignant melanoma.

Material and Methods

Materials

All chemical reagents utilized in this experimental study were procured from Sigma Chemicals Co. (USA), Scharlau Chemie Co. (Spain), and Merck Co. (Germany), and were employed without any further purification. Prior to experimental procedures, all glassware was meticulously cleansed using freshly prepared aqua regia, followed by thorough rinsing with Deionized (DI) water. DI water was consistently utilized for the preparation of all solutions and for final rinsing steps to ensure the elimination of potential contaminants throughout the experimental process.

Synthesis of AgB NCs

In this research, the aqueous extract of Rheum turkestanicum wood was prepared by subjecting finely powdered wood to continuous agitation in distilled water, followed by filtration to remove solid residues. For the synthesis of Ag-Bi_2O_3 nanocomposites (AgB NCs), 20 mL of the obtained plant extract was diluted with distilled water to a final volume of 50 mL and subsequently heated to 70 °C in a thermostatically controlled water bath. A precursor solution (50 mL) containing equimolar concentrations of $Bi(NO_3)_3{\bullet}5H_2O$ and $AgNO_3$ was then added dropwise to the heated extract under constant magnetic stirring. The reaction mixture was maintained under these conditions for 3 h to facilitate the formation of nanocomposites. The resulting suspension was then dried at 90 °C for 15 h, and the dried material was subjected to calcination at 500 °C for 2 h to yield the final AgB NCs.

Synthesis of FAgB NCs

To achieve functionalization of the AgB NCs with folic acid, 0.1 g of the synthesized AgB NCs was suspended in 50 mL of distilled water. A 2.5 mM folic acid solution was prepared and adjusted to pH 8.5 by adding 0.5 mM NaOH. This solution was introduced to the nanoparticle suspension and subjected to reflux at 90 °C for 4 h. The mixture was then dried at 90 °C for 10 h to obtain FAgB NCs.

Characterization of NCs

The synthesized nanocomposites were analyzed for their structural and physicochemical characteristics through various techniques. Field Emission Scanning Electron Microscopy (FESEM) images were captured using a ZEISS Sigma 300 instrument from Germany. UV-visible (UV-vis) absorption spectroscopy was conducted with a UV-1800 double-beam spectrophotometer manufactured by SHIMADZU in Japan. Additionally, Powder X-ray Diffraction (PXRD) analysis was performed utilizing a PANalytical X'Pert PRO MPD instrument from the Netherlands, employing Cu Kα radiation. Fourier Transform Infrared (FTIR) spectra were also recorded using a Perkin Elmer Spectrum 100 FTIR device from the USA.

Cell line preparation

C540 melanoma cells were obtained from the Pasteur Institute of Iran and cultured in Dulbecco's Modified Eagle Medium (DMEM) enriched with 10% Fetal Bovine Serum (FBS) and 1% penicillin-streptomycin (Gibco, USA) at a temperature of 37 °C within a humidified incubator containing 5% CO_2.

Assessment of cellular toxicity and sonodynamic therapy

In this investigation, C540 cells were cultured at a density of 1.0×10^4 cells in 96-well plates for a period of 24 h to facilitate cell adhesion. Subsequent to this, the cells were divided into two distinct groups: one group remained untreated with ultrasound (U-), while the other group received ultrasound treatment (U+). The cytotoxic and growth inhibitory effects of AgB and FAgB NCs on cancer cells were evaluated using the 3-(4,5-dimethylthiazol-2-yl)-2,5-diphenyltetrazolium bromide (MTT) assay. The cells were exposed to various concentrations (10-500 µg mL^{-1}) of AgBi and F-AgBi NCs. Initially, the culture medium was completely replaced with an MTT solution (0.5%, 100 µL) that had been solubilized in Phosphate-Buffered Saline (PBS), followed by an additional incubation period of 4 h. Afterward, 100 µL of dimethyl sulfoxide (DMSO) was added to replace the MTT solution, allowing for the solubilization of the MTT formazan crystals, which were then centrifuged at 3500 rpm for 3 min. The optical density of each well was measured at a wavelength of 570 nm using a microplate ELISA reader (Biotek, Winooski, VT, USA). To ensure the accuracy of the results, all measurements were conducted in triplicate. The control cells, which did not receive any treatment, were designated as having 100% viability, and cell survival was quantified using the following Equation 1 [8]:

$$\textbf{Cell survival=(Optical density of treated sample/Optical density of control sample)}\times\textbf{100} \quad (1)$$

In the U+ groups, following a one-hour incubation period, an ultrasonic instrument (215X, Novin, Iran) equipped with an unfocused planar U transducer was meticulously positioned in direct contact with the substrate of the cell culture plate. The calibration uncertainty was strictly maintained at a threshold of less than ±1 mW. The central axis of the planar transducer was meticulously aligned beneath each individual well, and irradiation was conducted at a power intensity of 1.0 W cm^{-2} for a duration of 5 min, employing a duty cycle of 50% and a frequency of 1 MHz. The U+ and U- treated cell cohorts were then subjected to an overnight incubation at a temperature of 37 °C, within an environment containing 5% CO_2.

Intracellular ROS production using NCs

The assay was conducted following the methodology outlined by Z. Kayani et al. [39]. In this investigation, 2′,7′-dichlorodihydrofluorescein diacetate (DCFH-DA) served as an indicator for intracellular ROS. C540 cells were cultured in 96-well plates and subsequently categorized into two groups: U- and U+ groups. These groups underwent treatment with AgB and FAgB NCs at a concentration of 50 µg mL^{-1}. After a 1 h incubation, 100 µL of a fresh DCFH-DA solution was introduced. Following an additional 30 min incubation, the U+ group was subjected to a frequency of 1 MHz and an output power of 1.0 W cm^{-2} with a 50% pulse ratio for 5 min. To remove any extracellular 2′,7′-dichlorodihydrofluorescein (DCF), the cells were washed three times with PBS. Subsequently, 100 µL of lysis buffer was added to each well, and after a 30 min incubation, the fluorescence emission intensity at 520 nm, following excitation at 485 nm, was measured in 96-well black plates using a microplate reader (Biotek, Winooski, VT, USA).

Extracellular ROS production using NCs

This assay was performed in accordance with the methodology outlined by Z. Kayani et al. [39] using H_2DCF (2′,7′-dichlorodihydrofluorescein) in the absence of cellular interactions. The preparation of H_2DCF involved the deacetylation of H_2DCF-DA. Specifically, 75 µL of H_2DCF solution was combined with 75 µL of AgB and FAgB NCs at a concentration of 50 µg mL^{-1} in a fluorescence cuvette. Subsequently, radiation from a source designated as “U” was applied at a frequency of 1.0 MHz, with a duty cycle of 50%. The radiation exposure time was set to 5 min. The fluorescence intensities of the samples were then measured using a Varian (USA) spectrofluorometer, with PBS serving as a control.

Apoptotic assay

The evaluation of apoptosis was conducted through a method known as Fluorescence-Activated Cell Sorting (FACS) analysis, utilizing annexin V-FITC (fluorescein isothiocyanate) and Propidium Iodide (PI) staining kits. C540 cells were grown in 12-well plates and divided into two separate groups: U+ and U-. After a

24-h incubation period, the cells were collected, rinsed with PBS, and stained with 10 µL of annexin V−FITC and 10 µL of PI. The analysis was carried out using a BD FACSCalibur Flow Cytometer from BD Biosciences (Franklin Lakes, NJ, USA). The quantification of apoptotic cells was determined based on the fluorescence signals from 10,000 analyzed events.

Scratch assay

In the scratch assay, C540 cells were inoculated into 24-well plates at a density of 2×10^5 cells mL^{-1} and incubated for 24 h at 37 °C in a 5% CO_2 atmosphere. Following this incubation period, a confluent monolayer of cells was observed. To induce the formation of scratches, the monolayer was meticulously scraped in a linear fashion. Subsequent to this, the cell debris was removed by washing the wells with a fresh culture medium. The cells were then subjected to incubation at 37 °C in the presence of AgB and FAgB NCs, both administered at concentrations of 50 µg mL^{-1}. The aforementioned NCs were also exposed to U irradiation. To observe the dynamics of cell migration over time, optical images of the scratched area were taken at fixed time intervals, namely at the initial time (t_0) and after 24 h, using a digital light microscope.

Evaluation of spheroid viability assay

C540 cells were subsequently introduced at a density of 1×10^4 cells per well in a 96-well plate and incubated in a humidified chamber at 37 °C with 5% CO_2. After a three-day incubation period, C540 spheroids were generated, and the wells were subjected to treatment with AgB and FAgB NCs at a concentration of 50 µg mL^{-1}, in addition to U-irradiation and a combination of both treatment modalities. All experimental conditions were preserved overnight at 37 °C in a humidified environment with a stable 5% CO_2 concentration. To guarantee the reliability and reproducibility of the results, each cell group was arranged in triplicate, with each treatment condition being repeated three times. The evaluation involved quantifying the fluorescence intensity of resazurin, using a Biotek microplate reader set to an excitation wavelength of 544 nm and an emission wavelength of 600 nm.

Statistical analysis

Data analysis was conducted utilizing GraphPad Prism 10 (GraphPad Software, San Diego, CA, USA). The paired sample comparisons were assessed using the Student's t-test, whereas one-way ANOVA was applied to evaluate differences across multiple groups. The results are presented as mean ± Standard Deviation (SD), with statistical significance established at $P\leq0.05$.

Results

PXRD

The PXRD patterns of AgB and FAgB nanocomposites are shown in Figure 1a. Both materials exhibit characteristic diffraction peaks at 2θ values of 21.89°, 24.66°, 25.86°, 27.03°, 27.52°, 28.11°, 33.30°, 35.53°, 37.08°, 40.17°, 45.25°, 46.45°, 48.66°, 52.47°, 54.91°, 57.96°, and 63.64°, which correspond to the monoclinic α-Bi_2O_3 phase (JCPDS No. 71-0465). These results are consistent with prior studies on doped α-Bi_2O_3 structures [40]. Additional peaks at $2\theta=37.72°$, 44.40°, and 64.51° in the AgB pattern confirm the presence of metallic silver (Ag) (ICSD Card No. 52362) [41]. The size of the crystallites was determined utilizing the Debye-Scherrer formula, as outlined in Equation 2 [42]:

$$D=K\lambda/(\beta\cos\theta) \qquad (2)$$

In this context, D represents the mean crystallite size, K denotes the shape factor, λ indicates the wavelength of the X-ray, β refers to the Full Width at Half Maximum (FWHM), and θ signifies the Bragg angle [42]. The average crystallite sizes were estimated to be 57.84 nm for AgB NCs and 68.84 nm for FAgB NCs. The slight increase in crystallite size after folic acid conjugation suggests that folic acid may have influenced particle growth during synthesis.

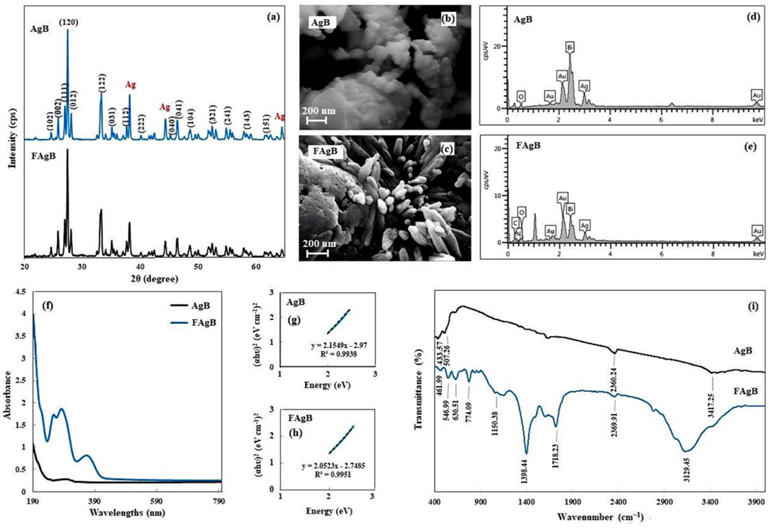

Figure 1: (**a**) Powder X-ray Diffraction (PXRD) spectra, (**b**) and (**c**) Field Emission Scanning Electron Microscopy (FESEM) images, (**d**) and (**e**) Energy-Dispersive X-ray spectroscopy (EDX), (**f**) UV–vis absorption spectra, (**g**) and (**h**) band- gap, and (**i**) Fourier Transform Infrared (FTIR) spectra of silver-bismuth oxide nanocomposites (AgB NCs) and folic acid-functionalized counterparts (FAgB NCs).

FESEM and Energy-Dispersive X-ray spectroscopy (EDX)

FESEM images of AgB and FAgB NCs (Figures 1b and c) reveal differences in morphology. AgB NCs displayed a porous, irregular surface, whereas FAgB NCs exhibited distinct tentacle-like structures with lengths of ~500-600 nm and diameters of ~30-40 nm, indicating a morphological shift due to folic acid coating.

The elemental composition was verified using EDX as illustrated in Figures 1d and e. The AgB NCs were found to contain silver (Ag), bismuth (Bi), and oxygen (O). In contrast, the FAgB NCs also displayed the presence of carbon (C) and nitrogen (N), suggesting the functionalization with folic acid. The detection of C and N atoms serves as evidence for the successful attachment of folic acid to the surface of the AgB NCs.

UV-vis absorption

UV–vis absorption spectra (Figure 1f) show a weak absorption peak at 298 nm for AgB NCs, attributed to surface plasmon resonance (SPR) of Ag nanoparticles [43]. A blue shift of this peak in FAgB NCs indicates an altered electronic environment due to folic acid binding. The optical band gap energies of AgB and FAgB NCs were calculated using Tauc plots (Figure 1g and h), based on Equation 3 [50]:

$$(\alpha h\nu)^2 = A(h\nu - Eg) \qquad (3)$$

Where α is the absorption coefficient, $h\nu$ is photon energy, and Eg is the band gap energy [44]. The band gaps were found to be 1.37 eV for AgB and 1.33 eV for FAgB NCs. The reduced band gap in FAgB NCs suggests improved electronic transitions and better sonoabsorbing activity.

FTIR

FTIR spectra of AgB and FAgB NCs are shown in Figure 1i. For AgB NCs, characteristic Bi-O and Ag-O stretching vibrations appeared at 433, 507 cm^{-1} and 461, 546 cm^{-1}, respectively [45,46]. These characteristic peaks were also observed in FAgB NCs, confirming the presence of folic acid functional groups such as strong peaks at 1398, 1618, and 1718 cm^{-1} corresponding to C=C, C=O stretching, and N–H bending vibrations. The incorporation of folic acid is further supported by additional signals consistent with its molecular structure, verifying successful conjugation to the nanocomposite surface [47].

Cytotoxicity and U-Assisted Therapy

The cytotoxic effects were assessed using MTT assays on C540 melanoma cells subjected to escalating concentrations (10-500 μg mL^{-1}) of AgB and FAgB NCs. As illustrated in Figure 2a, both NCs exhibited dose-dependent cytotoxicity, with FAgB NCs showing significantly higher potency. At 50 μg mL^{-1}, cell viability dropped to 61.81% for AgB and 48.42% for FAgB NCs. The calculated IC_{50} values were 76.95 μg mL^{-1} (AgB) and 28.58 μg mL^{-1} (FAgB), highlighting the enhanced therapeutic effect of folic acid functionalization. U exposure (1 MHz, 1.0 W cm^{-2}, 5 min) further reduced cell viability (Figure 2b). The combination treatment (FAgB/U^+) led to the most pronounced cytotoxic effect, reducing viability to 27.58%, compared to 42.12% for AgB/U+.

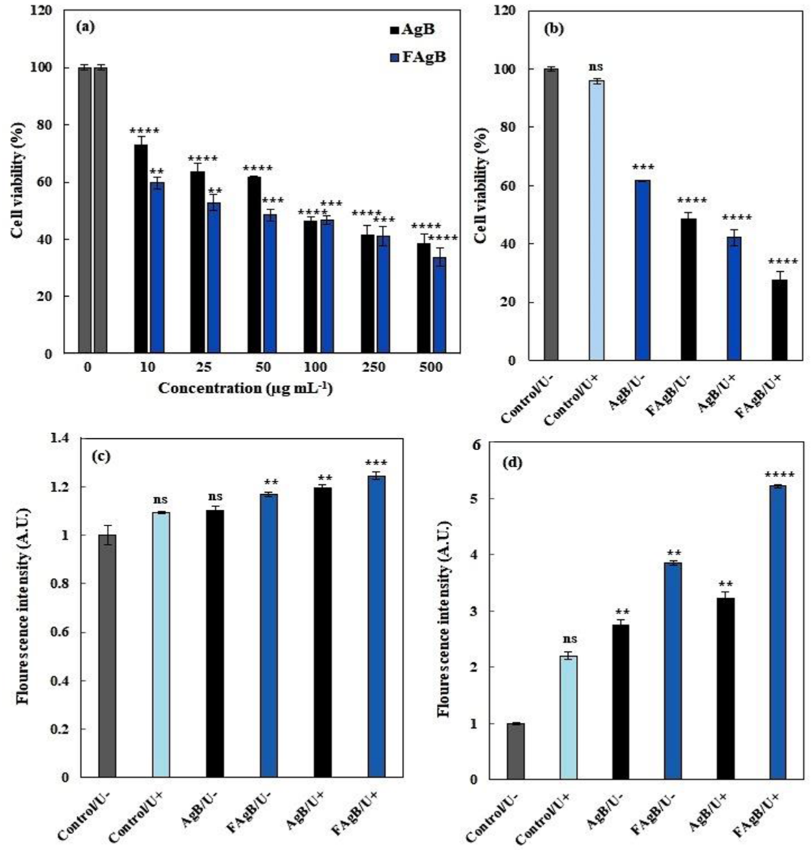

Figure 2: (**a**) And (**b**) *In vitro* viability percents of C540 cells treated in different groups (un-exposure of ultrasound (U) (**a**), and exposure of ultrasound (U) irradiation (**b**)); Fluorescence intensities of 2′,7′-dichlorodihydrofluorescein (H2-DCF) in control samples of silver-bismuth oxide nanocomposites (AgB NCs) and folic acid-functionalized counterparts (FAgB NCs) (50 μg mL^{-1}) exposure of Ultrasound (U) radiation at 50% pulse ratios over duration of 5 minutes, presented in (**c**) under cell-free conditions and (**d**) within C540 cells. The error bars represent the standard deviations derived from three independent measurements. ** indicate significant differences (*P*-value=0.001), *** and **** indicates very significant differences (*P*-value<0.0001). The error bars represent the standard deviations derived from three independent measurements.

Reactive Oxygen Species (ROS) Generation

The ability of NCs to induce ROS was measured via fluorescence emission of oxidized DCF. As shown in Figure 2c, both AgB and FAgB NCs induced ROS production in extracellular media, but FAgB NCs showed significantly higher levels, especially under US exposure. Similarly, intracellular ROS assays (Figure 2d) revealed that U^+ treatment alone modestly increased oxidative stress, while FAgB/U+ led to the highest ROS levels. These findings demonstrate the synergistic effect of folic acid conjugation and U exposure, which enhances ROS generation through suppressed electron-hole recombination and improved cellular uptake [48,49].

Apoptosis Induction

Flow cytometric analysis using Annexin V-FITC/PI staining was employed to quantify apoptosis (Figure 3b). The FAgB/U+ group showed the highest apoptosis rates (95.4%), followed by FAgB/U- (95.46%), AgB/U+ (26.1%), and AgB/U- (22.4%). The substantial apoptotic response in FAgB/U+ suggests enhanced mitochondrial dysfunction and ROS-mediated DNA damage.

The quadrants in the dot plots represent in Figure 3a:

- Q1: necrotic ($PI^+/FITC^-$)
- Q2: late apoptotic ($PI^+/FITC^+$)
- Q3: early apoptotic ($PI^-/FITC^+$)
- Q4: viable cells ($PI^-/FITC^-$)

These results align with earlier cytotoxicity

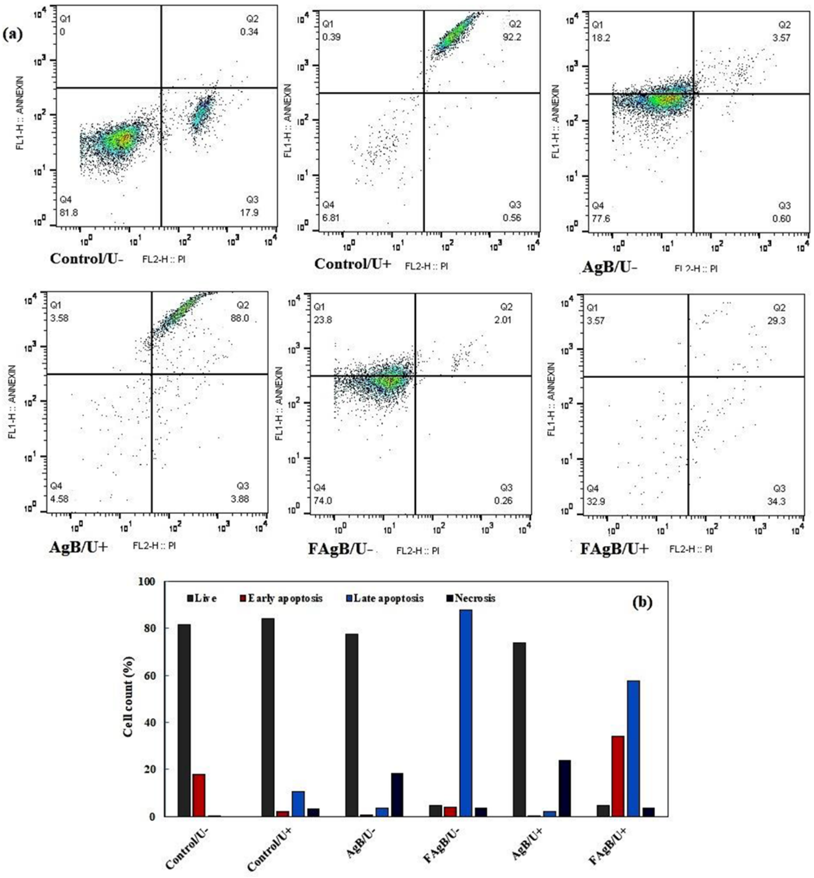

Figure 3: (**a**) Flow cytometric assessment of apoptotic impacts of silver-bismuth oxide nanocomposites (AgB NCs) and folic acid-functionalized counterparts (FAgB NCs) exposure and unexposure of Ultrasound (U) radiation, and (**b**) The viability percentages of live, early apoptotic, late apoptotic, and necrotic of C540 cells across various treatment groups.

and ROS data, confirming that the synergistic application of FAgB NCs and US significantly promotes apoptosis in melanoma cells.

Cell migration

The scratch assay was conducted to assess cell motility after treatment with AgB and FAgB NCs (Figure 4). After 24 h, untreated control cells showed substantial wound closure, while cells exposed to NCs and U (especially FAgB/U+) demonstrated markedly reduced migration. The combined effect of U and NCs significantly inhibited cell mobility. Folic acid enhanced this inhibitory effect, possibly due to its role in modulating redox balance and cellular adhesion processes. These findings highlight the capacity of FAgB NCs to hinder metastatic activity in melanoma cells.

Spheroid formation

Three-dimensional (3D) spheroid cultures better mimic thin vivo tumor microenvironment. After 3 days of incubation, treatment with NCs led to significant decreases in spheroid viability. Viability reductions were 33.31% (AgB/U$^-$), 39.59% (FAgB/U$^-$), 42.58% (AgB/U+), and 47.01% (FAgB/U+) (Figure 5). U exposure further amplified the therapeutic effect, likely via increased cavitation and localized ROS production. Folic acid functionalization also contributed to deeper nanoparticle penetration and enhanced apoptosis. These results validate the ability of FAgB NCs to suppress tumor growth in complex 3D models.

Discussion

The size, shape, and surface characteristics of nanosystems designed for cancer therapy play a crucial role in how they behave inside the body and ultimately determine their effectiveness against tumors. In our study, the folic acid-functionalized AgB nanocomposites (FAgB NCs) had an average diameter of around 30-40 nm. The alteration shape of FAgB compared to Ag-Bi and also FTIR, UV-vis absorption and PXRD confirmed the successful incorporation of folic acid onto the nanoparticle surface. Since normal blood vessels have pores smaller than 12 nm, previous research has shown that nanoparticles above this size tend to accumulate preferentially in tumor tissues, thanks to the Enhanced Permeability and Retention (EPR) effect [50]. Therefore, keeping nanoparticles within the roughly 12-60 nm size range seems ideal for effective tumor penetration and cellular uptake. UV-vis analysis showed that both AgB and FAgB NCs have significantly narrower band gaps compared to α-Bi_2O_3 nanorods (which have 3.55 eV) [51]. This narrower

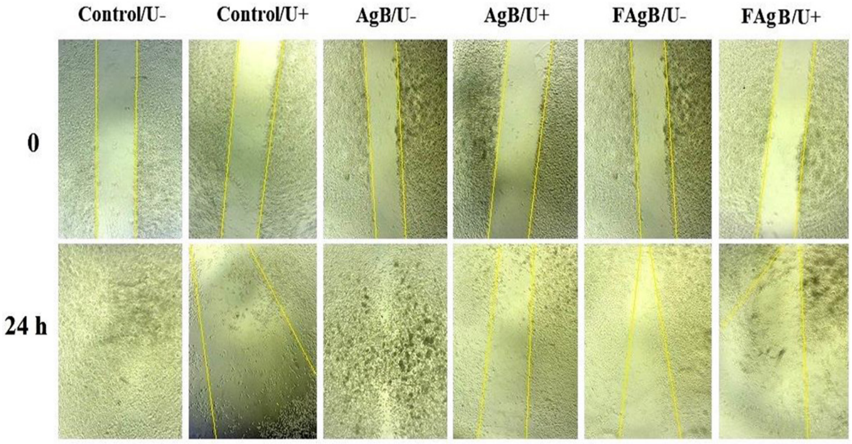

Figure 4: Cellular Migration-Scratch assay of silver-bismuth oxide nanocomposites (AgB NCs) and folic acid-functionalized counterparts (FAgB NCs) using C540 cells at different treatment groups.

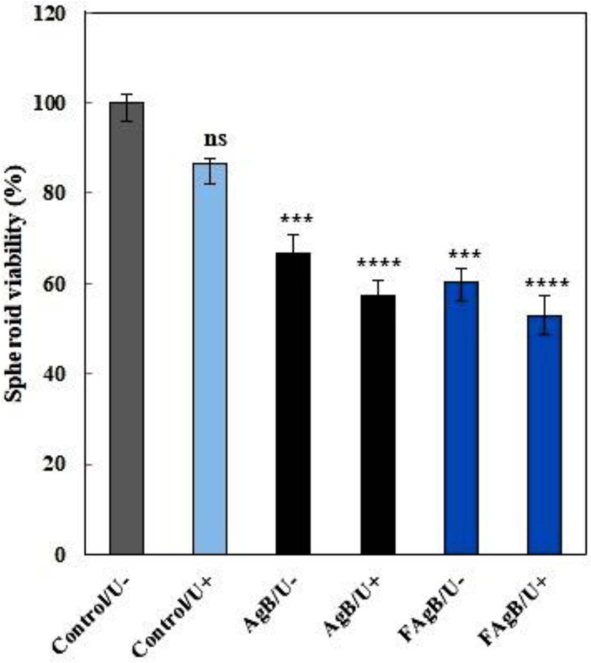

Figure 5: Spheroid viability percent's of C540 cells treated in silver-bismuth oxide nanocomposites (AgB NCs) and folic acid-functionalized counterparts (FAgB NCs). *** And **** indicate very significant difference (*P*-value<0.0001).

band gap helps reduce the rapid recombination of photoexcited electron-hole pairs, which in turn boosts the generation of ROS. This effect was evident in our experiments, where the sonosensitizing ability of AgB and especially FAgB NCs was significantly improved when combined with U. We observed greater cell killing and apoptosis in melanoma cells treated with the nanocomposites plus U compared to either treatment alone. The enhanced efficacy of FAgB NCs can likely be attributed to folate receptor-mediated endocytosis, which promotes higher intracellular accumulation and increased ROS production. Looking closer at the mechanism, the reduced band gap in these nanocomposites' aids in efficient charge separation. Incorporating silver into Bi_2O_3 extends the lifetime of electron-hole pairs, thereby improving the sonocatalytic reaction. This leads to abundant generation of ROS, including singlet oxygen, superoxide radicals, and hydroxyl radicals, which cause oxidative damage to critical cellular components. This oxidative stress results in protein inactivation and cross-linking, along with DNA strand breaks, ultimately triggering cell death.

Inasmuch 3D cell spheroids maintain more complex cell–cell and cell–matrix interactions as well as oxygen and nutrient gradients, thus they better replicate the tumor microenvironment compared to traditional 2D cultures. The hypoxic conditions often found in spheroids can reduce ROS production and diminish the effectiveness of SDT, which helps explain why we observed somewhat lower cytotoxicity in the 3D models [52]. However, our experiments showed that under U, FAgB NCs enhanced cavitation effects, which improved their penetration and therapeutic impact even in these more challenging 3D environments.

Finally, since cell migration is a critical factor in melanoma metastasis, we performed scratch assays and found that treatment with FAgB NCs significantly inhibited melanoma cell migration. This points to a promising anti-metastatic potential, which is especially important given melanoma's high tendency to spread to secondary sites like the lungs.

Despite the promising results demonstrated by FAgB NCs as effective sonosensitizers for melanoma treatment, several limitations should be acknowledged. First, while *in vitro* 2D and 3D cell culture models provide valuable insights into therapeutic efficacy and tumor microenvironment interactions, they cannot fully replicate the complexity of *in vivo* model, including immune response, pharmacokinetics, and biodistribution. Also, the long-term biocompatibility, systemic toxicity, and clearance of these nanocomposites remain unsolved. Future research should focus on *in vivo* validation of therapeutic efficacy and safety in melanoma animal models. Integration with other treatment modalities and evaluation against a broader range of tumor types would also be valuable for translating these nanomaterials into clinical applications.

Conclusion

In this study, we successfully developed and characterized AgB NCs and their folic acid-functionalized form (FAgB NCs) using *Rheum turkestanicum* extract as a green, eco-friendly reducing agent. Structural and morphological analyses confirmed the integrity of the nanocomposites and the successful functionalization with folic acid, which significantly modified their surface characteristics, reduced band gap energy, and improved their optical and catalytic properties, which facilitated ROS production. Biological assays revealed that both nanocomposites displayed potent, dose-dependent cytotoxic effects against C540 melanoma cells. Importantly, FAgB NCs showed significantly greater efficacy, with lower IC_{50} values, likely due to folate receptor-mediated endocytosis that promoted selective cellular uptake.

Upon U activation, both nanocomposites functioned as effective sonosensitizers, amplifying intracellular and extracellular ROS production, disrupting mitochondrial function, and inducing apoptosis. FACS analysis confirmed that FAgB NCs under SDT induced a dramatic increase in both early and late apoptotic cell populations. Furthermore, FAgB NCs significantly inhibited cell migration and suppressed spheroid growth in 3D tumor models, underscoring their potential for deep-tissue tumor ablation.

These findings highlight the functionality of FAgB NCs as U-activated sonosensitizer. The integration of folic acid not only enhances tumor-specific targeting but also promotes ROS-mediated cytotoxicity, positioning this nanocomposite as a promising platform for non-invasive cancer therapy.

Acknowledgment

The paper has been extracted from M. Sarani's PhD thesis supported by the Research Council of Shiraz University of Medical Sciences.

Authors' Contribution

Regarding the authors' contributions, N. Sattarahmady contributed to conceptualization, funding acquisition, project administration, supervision, validation, writing- review & editing, and M. Sarani contributed to the study conception, data curation, analysis, investigation, and writing- original draft. H. Haghighi played a pivotal role in designing the procedure. H. Heli and P. Tamaddon contributed to formal analysis, validation and writing- review & editing. MR. Sardashti Birjandi and Z. Kayani, played a pivotal role in material preparation, Data analysis were performed by M. Sarani, H. Haghighi, A. Safari, M. Darroudi, and GH. Tondro. All authors read, modified, and approved the final version of the manuscript.

Ethical Approval

The national ethics committee confirmed the study with the ethical code of IR.SUMS.REC.1403.113. We did not perform any intervention in therapeutic procedures. Therefore, gathering the consent forms was waived due to the nature of this study.

Funding

This work was supported by Shiraz University of Medical Sciences (Shiraz, Iran) with the grant number of "29875".

Conflict of Interest

N. Sattarahmady, as the Editorial Board Member, was not involved in the peer-review and decision-making processes for this manuscript.

References

1. Madamsetty VS, Paul MK, Mukherjee A, Mukherjee S. Functionalization of Nanomaterials and Their Application in Melanoma Cancer Theranostics. *ACS Biomater Sci Eng.* 2020;**6**(1):167-81. doi: 10.1021/acsbiomaterials.9b01426. PubMed PMID: 33463233.
2. Kashyap BK, Singh VV, Solanki MK, Kumar A, Ruokolainen J, Kesari KK. Smart Nanomaterials in Cancer Theranostics: Challenges and Opportunities. *ACS Omega*. 2023;**8**(16):14290-320. doi: 10.1021/acsomega.2c07840. PubMed PMID:

37125102. PubMed PMCID: PMC10134471.

3. Chandra J, Hasan N, Nasir N, Wahab S, Thanikachalam PV, Sahebkar A, et al. Nanotechnology-empowered strategies in treatment of skin cancer. *Environ Res*. 2023;**235**:116649. doi: 10.1016/j.envres.2023.116649. PubMed PMID: 37451568.
4. Orthaber K, Pristovnik M, Skok K, Perić B, Maver U. Skin cancer and its treatment: novel treatment approaches with emphasis on nanotechnology. *J Nanomater*. 2017;*2017*(1):1-20.
5. Wunderlich K, Suppa M, Gandini S, Lipski J, White JM, Del Marmol V. Risk Factors and Innovations in Risk Assessment for Melanoma, Basal Cell Carcinoma, and Squamous Cell Carcinoma. *Cancers (Basel)*. 2024;**16**(5):1016. doi: 10.3390/cancers16051016. PubMed PMID: 38473375. PubMed PMCID: PMC10931186.
6. Huang L, Zuo Y, Li S, Li C. Melanocyte stem cells in the skin: Origin, biological characteristics, homeostatic maintenance and therapeutic potential. *Clin Transl Med*. 2024;**14**(5):e1720. doi: 10.1002/ctm2.1720. PubMed PMID: 38778457. PubMed PMCID: PMC11111606.
7. Touni AA, Shivde RS, Echuri H, Abdel-Aziz RTA, Abdel-Wahab H, Kundu RV, Le Poole IC. Melanocyte-keratinocyte cross-talk in vitiligo. *Front Med (Lausanne)*. 2023;**10**:1176781. doi: 10.3389/fmed.2023.1176781. PubMed PMID: 37275386. PubMed PMCID: PMC10235633.
8. Kayani Z, Dehdari Vais R, Soratijahromi E, Mohammadi S, Sattarahmady N. Curcumin-gold-polyethylene glycol nanoparticles as a nanosensitizer for photothermal and sonodynamic therapies: In vitro and animal model studies. *Photodiagnosis Photodyn Ther*. 2021;**33**:102139. doi: 10.1016/j.pdpdt.2020.102139. PubMed PMID: 33310015.
9. Sattarahmady N, Kayani Z, Heli H, Faghani-Eskandarkolaei P, Haghighi H. Photosensitizing Activity of Nanoparticles of Poly (2-amino phenol)/Gold for Intensified Doxorubicin Therapeutic Effect on Melanoma Cancer Cells under Synergism Effect of 808-nm Light. *J Biomed Phys Eng*. 2024;**14**(6):547-60. doi: 10.31661/jbpe.v0i0.2312-1693. PubMed PMID: 39726887. PubMed PMCID: PMC11668927.
10. Zahraie N, Haghighi H, Salehi F, Daneshvar F, Tamaddon P, Sattarahmady N. Pulsed sonodynamic therapy of melanoma cancer cells using nanoparticles of and mesoporous platinum. *Ultrasound Med Biol*. 2023;**49**(9):2160-8. doi: 10.1016/j.ultrasmedbio.2023.06.011. PubMed PMID: 37414634.
11. Gong Z, Dai Z. Design and Challenges of Sonodynamic Therapy System for Cancer Theranostics: From Equipment to Sensitizers. *Adv Sci (Weinh)*. 2021;**8**(10):2002178. doi: 10.1002/advs.202002178. PubMed PMID: 34026428. PubMed PMCID: PMC8132157.
12. Yu Y, Liu S, Yang L, Song P, Liu Z, Liu X, Yan X, Dong Q. Roles of reactive oxygen species in inflammation and cancer. *MedComm (2020)*. 2024;**5**(4):e519. doi: 10.1002/mco2.519. PubMed PMID: 38576456. PubMed PMCID: PMC10993368.
13. Mustafa M, Ahmad R, Tantry IQ, Ahmad W, Siddiqui S, Alam M, et al. Apoptosis: A Comprehensive Overview of Signaling Pathways, Morphological Changes, and Physiological Significance and Therapeutic Implications. *Cells*. 2024;**13**(22):1838. doi: 10.3390/cells13221838. PubMed PMID: 39594587. PubMed PMCID: PMC11592877.
14. Simsek Papur O, Glatz JFC, Luiken JJFP. Protein kinase-D1 and downstream signaling mechanisms involved in GLUT4 translocation in cardiac muscle. *Biochim Biophys Acta Mol Cell Res*. 2024;**1871**(6):119748. doi: 10.1016/j.bbamcr.2024.119748. PubMed PMID: 38723678.
15. Yu M, Wang Z, Wang D, Aierxi M, Ma Z, Wang Y. Oxidative stress following spinal cord injury: From molecular mechanisms to therapeutic targets. *J Neurosci Res*. 2023;**101**(10):1538-54. doi: 10.1002/jnr.25221. PubMed PMID: 37272728.
16. Herwig M, Begovic M, Budde H, Delalat S, Zhazykbayeva S, Sieme M, et al. Protein Kinase D Plays a Crucial Role in Maintaining Cardiac Homeostasis by Regulating Post-Translational Modifications of Myofilament Proteins. *Int J Mol Sci*. 2024;**25**(5):2790. doi: 10.3390/ijms25052790. PubMed PMID: 38474037. PubMed PMCID: PMC10932171.
17. Nanzai B, Mochizuki A, Wakikawa Y, Masuda Y, Oshio T, Yagishita K. Sonoluminescence intensity and ultrasonic cavitation temperature in organic solvents: Effects of generated radicals. *Ultrason Sonochem*. 2023;**95**:106357. doi: 10.1016/j.ultsonch.2023.106357.
18. Aebisher D, Serafin I, Batóg-Szczęch K, Dynarowicz K, Chodurek E, Kawczyk-Krupka A, Bartusik-Aebisher D. Photodynamic Therapy in the Treatment of Cancer-The Selection of Synthetic Photosensitizers. *Pharmaceuticals (Basel)*. 2024;**17**(7):932. doi: 10.3390/ph17070932. PubMed PMID: 39065781. PubMed PMCID: PMC11279632.
19. Ma A, Ran H, Wang J, Ding R, Lu C, Liu L, et al. An Urchin-Shaped Copper-Based Metalloporphyrin Nanosystem as a Sonosensitizer for Sonodynamic Therapy. *Nanomaterials (Basel)*. 2022;**12**(2):209. doi: 10.3390/nano12020209. PubMed PMID:

35055229. PubMed PMCID: PMC8781994.

20. Teranishi R, Matsuda T, Yuba E, Kono K, Harada A. Sonodynamic Therapeutic Effects of Sonosensitizers with Different Intracellular Distribution Delivered by Hollow Nanocapsules Exhibiting Cytosol Specific Release. *Macromol Biosci.* 2019;**19**(4):e1800365. doi: 10.1002/mabi.201800365. PubMed PMID: 30707494.
21. Zhang X, He N, Zhang L, Dai T, Sun Z, Shi Y, et al. Application of high intensity focused ultrasound combined with nanomaterials in anti-tumor therapy. *Drug Deliv.* 2024;**31**(1):2342844. doi: 10.1080/10717544.2024.2342844. PubMed PMID: 38659328. PubMed PMCID: PMC11047217.
22. Yang N, Li J, Yu S, Xia G, Li D, Yuan L, et al. Application of Nanomaterial-Based Sonodynamic Therapy in Tumor Therapy. *Pharmaceutics.* 2024;**16**(5):603. doi: 10.3390/pharmaceutics16050603. PubMed PMID: 38794265. PubMed PMCID: PMC11125068.
23. Sun S, Wang P, Sun S, Liang X. Applications of Micro/Nanotechnology in Ultrasound-based Drug Delivery and Therapy for Tumor. *Curr Med Chem.* 2021;**28**(3):525-47. doi: 10.2174/0929867327666200212100257. PubMed PMID: 32048951.
24. Li L, Lin H, Li D, Zeng Y, Liu G. Ultrasound activated nanosensitizers for sonodynamic therapy and theranostics. *Biomed Mater.* 2021;**16**(2):022008. doi: 10.1088/1748-605X/abd382. PubMed PMID: 33316792.
25. Wang J, Zhao Z, Liu Y, Cao X, Li F, Ran H, et al. ‘Mito-Bomb’: a novel mitochondria-targeting nanosystem for ferroptosis-boosted sonodynamic antitumor therapy. *Drug Deliv.* 2022;**29**(1):3111-22. doi: 10.1080/10717544.2022.2126027. PubMed PMID: 36131565. PubMed PMCID: PMC9518294.
26. Shahbazi MA, Faghfouri L, Ferreira MPA, Figueiredo P, Maleki H, Sefat F, et al. The versatile biomedical applications of bismuth-based nanoparticles and composites: therapeutic, diagnostic, biosensing, and regenerative properties. *Chem Soc Rev.* 2020;**49**(4):1253-321. doi: 10.1039/c9cs00283a. PubMed PMID: 31998912.
27. Gao F, Wang D, Zhang T, Ghosal A, Guo Z, Miao Y, et al. Facile synthesis of Bi2S3-MoS2 heterogeneous nanoagent as dual functional radiosensitizer for triple negative breast cancer theranostics. *Chem Eng J Adv.* 2020;**395**:125032. doi: 10.1016/j.cej.2020.125032.
28. Song K, Chen G, He Z, Shen J, Ping J, Li Y, et al. Protoporphyrin-sensitized degradable bismuth nanoformulations for enhanced sonodynamic oncotherapy. *Acta Biomater.* 2023;**158**:637-48. doi: 10.1016/j.actbio.2022.12.065. PubMed PMID: 36621634.
29. Lateef R, Ahmad I, Mahdi AA, Lohia N, Alhadlaq HA, Akhtar MJ, Ahamed M. Toxic Effects of Synthesized Bismuth Oxide/Reduced Graphene Oxide (Bi2O3/RGO) Nanocomposites in Two Distinct Mammalian Cell Lines: Role Oxidative Stress and Apoptosis. *Int J Nanomedicine.* 2024;**19**:12655-74. doi: 10.2147/IJN.S489874. PubMed PMID: 39619053. PubMed PMCID: PMC11608047.
30. Li Z, Hu Y, Miao Z, Xu H, Li C, Zhao Y, et al. Dual-Stimuli Responsive Bismuth Nanoraspberries for Multimodal Imaging and Combined Cancer Therapy. *Nano Lett.* 2018;**18**(11):6778-88. doi: 10.1021/acs.nanolett.8b02639. PubMed PMID: 30288978.
31. Zhou R, Liu X, Wu Y, Xiang H, Cao J, Li Y, et al. Suppressing the Radiation-Induced Corrosion of Bismuth Nanoparticles for Enhanced Synergistic Cancer Radiophototherapy. *ACS Nano.* 2020;**14**(10):13016-29. doi: 10.1021/acsnano.0c04375. PubMed PMID: 32898419.
32. Luceri A, Francese R, Lembo D, Ferraris M, Balagna C. Silver Nanoparticles: Review of Antiviral Properties, Mechanism of Action and Applications. *Microorganisms.* 2023;**11**(3):629. doi: 10.3390/microorganisms11030629. PubMed PMID: 36985203. PubMed PMCID: PMC10056906.
33. Muddassir M, Raza A, Munir S, Basirat A, Ahmed M, Butt MS, et al. Antibacterial efficacy of silver nanoparticles (AgNPs) against metallo-β-lactamase and extended spectrum β-lactamase producing clinically procured isolates of Pseudomonas aeruginosa. *Sci Rep.* 2022;**12**(1):20685. doi: 10.1038/s41598-022-24531-9. PubMed PMID: 36450765. PubMed PMCID: PMC9712613.
34. Zeng L, Gowda BHJ, Ahmed MG, Abourehab MAS, Chen ZS, Zhang C, et al. Advancements in nanoparticle-based treatment approaches for skin cancer therapy. *Mol Cancer.* 2023;**22**(1):10. doi: 10.1186/s12943-022-01708-4. PubMed PMID: 36635761. PubMed PMCID: PMC9835394.
35. Karunakar KK, Cheriyan BV, Krithikeshvaran R, Gnanisha M, Abinavi B. “Therapeutic advancements in nanomedicine: The multifaceted roles of silver nanoparticles”. *Biotechnol Notes.* 2024;**5**:64-79. doi: 10.1016/j.biotno.2024.05.002. PubMed PMID: 39416696. PubMed PMCID: PMC11446369.
36. Al-Thani AN, Jan AG, Abbas M, Geetha M, Sadasivuni KK. Nanoparticles in cancer theragnostic and drug delivery: A comprehensive review. *Life Sci.* 2024;**352**:122899. doi: 10.1016/j.lfs.2024.122899. PubMed PMID: 38992574.
37. Ramezani F, Moghadasi M, Shamsasen-

jan K, Narmani A. Folic Acid-Decorated Chitosan-PLGA Nanobiopolymers for Targeted Drug Delivery to Acute Lymphoblastic Leukemia Cells: In Vitro Studies. *Technol Cancer Res Treat.* 2024;**23**:15330338241308077. doi: 10.1177/15330338241308077. PubMed PMID: 39711084. PubMed PMCID: PMC11672380.

38. El-Borady OM, El-Sayed AF. Synthesis, morphological, spectral and thermal studies for folic acid conjugated ZnO nanoparticles: potency for multi-functional bio-nanocomposite as antimicrobial, antioxidant and photocatalytic agent. *J Mater Res Tech.* 2020;**9**(2):1905-17. doi: 10.1016/j.jmrt.2019.12.022.
39. Kayani Z, Heli H, Dehdari Vais R, Haghighi H, Ajdari M, Sattarahmady N. Synchronized Chemotherapy/Photothermal Therapy/Sonodynamic Therapy of Human Triple-Negative and Estrogen Receptor-Positive Breast Cancer Cells Using a Doxorubicin-Gold Nanoclusters-Albumin Nanobioconjugate. *Ultrasound Med Biol.* 2024;**50**(6):869-81. doi: 10.1016/j.ultrasmedbio.2024.02.012. PubMed PMID: 38538442.
40. Viruthagiri G, Kannan P, Shanmugam N. Photocatalytic rendition of Zn2+-doped Bi2O3 nanoparticles. *Photonics Nanostruct.* 2018;**32**:35-41. doi:10.1016/j.photonics.2018.05.008.
41. Ali MH, Azad MAK, Khan KA, Rahman MO, Chakma U, Kumer A. Analysis of Crystallographic Structures and Properties of Silver Nanoparticles Synthesized Using PKL Extract and Nanoscale Characterization Techniques. *ACS Omega.* 2023;**8**(31):28133-42. doi: 10.1021/acsomega.3c01261. PubMed PMID: 37576647. PubMed PMCID: PMC10413482.
42. Sarani M, Hamidian K, Barani M, Adeli-Sardou M, Khonakdar HA. α-Fe2 O3 @Ag and Fe3 O4 @Ag Core-Shell Nanoparticles: Green Synthesis, Magnetic Properties and Cytotoxic Performance. *ChemistryOpen.* 2023;**12**(6):e202200250. doi: 10.1002/open.202200250. PubMed PMID: 37260410. PubMed PMCID: PMC10235882.
43. Ruby, Aryan, Mehata MS. Surface plasmon resonance allied applications of silver nanoflowers synthesized from Breynia vitis-idaea leaf extract. *Dalton Trans.* 2022;**51**(7):2726-36. doi: 10.1039/d1dt03592d. PubMed PMID: 35080554.
44. Mohan AC, Athira A, Nair BP, Sivasubramanian G, Sreekanth KM, Anoop G, et al. Multifaceted properties of Ni and Zn codoped MgO nanoparticles. *Sci Rep.* 2024;**14**(1):32067. doi: 10.1038/s41598-024-83779-5. PubMed PMID: 39738509. PubMed PMCID: PMC11685388.
45. Sawaira Alsaiari M, Ahmad M, Munir M, Zafar M, Sultana S, Dawood S, et al. Efficient application of newly synthesized green Bi2O3 nanoparticles for sustainable biodiesel production via membrane reactor. *Chemosphere.* 2023;**310**:136838. doi: 10.1016/j.chemosphere.2022.136838. PubMed PMID: 36244423.
46. Singh P, Mijakovic I. Strong Antimicrobial Activity of Silver Nanoparticles Obtained by the Green Synthesis in Viridibacillus sp. Extracts. *Front Microbiol.* 2022;**13**:820048. doi: 10.3389/fmicb.2022.820048. PubMed PMID: 35250934. PubMed PMCID: PMC8888960.
47. Zhao X, Zhang J, Shi L, Xian M, Dong C, Shuang S. Folic acid-conjugated carbon dots as green fluorescent probes based on cellular targeting imaging for recognizing cancer cells. *RSC Advances.* 2017;**7**(67):42159-67. doi: 10.1039/C7RA07002K.
48. Komazec B, Cvjetko P, Balen B, Letofsky-Papst I, Lyons DM, Peharec Štefanić P. The Occurrence of Oxidative Stress Induced by Silver Nanoparticles in Chlorella vulgaris Depends on the Surface-Stabilizing Agent. *Nanomaterials (Basel).* 2023;**13**(13):1967. doi: 10.3390/nano13131967. PubMed PMID: 37446486. PubMed PMCID: PMC10343332.
49. Zhou J, Fang C, Rong C, Luo T, Liu J, Zhang K. Reactive oxygen species-sensitive materials: A promising strategy for regulating inflammation and favoring tissue regeneration. *Smart Mater Med.* 2023;**4**:427-46. doi: 10.1016/j.smaim.2023.01.004.
50. Haghighi H, Zahraie N, Haghani M, Heli H, Sattarahmady N. An amplified sonodynamic therapy by a nanohybrid of titanium dioxide-gold-polyethylene glycol-curcumin: HeLa cancer cells treatment in 2D monolayer and 3D spheroid models. *Ultrason Sonochem.* 2024;**102**:106747. doi: 10.1016/j.ultsonch.2023.106747. PubMed PMID: 38154206. PubMed PMCID: PMC10765485.
51. Abu-Dief AM, Mohamed WS. α-Bi2O3 nanorods: synthesis, characterization and UV-photocatalytic activity. *Mater Res Express.* 2017;**4**(3):035039. doi: 10.1088/2053-1591/aa6712.
52. Pereira PMR, Berisha N, Bhupathiraju NVSDK, Fernandes R, Tomé JPC, Drain CM. Cancer cell spheroids are a better screen for the photodynamic efficiency of glycosylated photosensitizers. *PLoS One.* 2017;**12**(5):e0177737. doi: 10.1371/journal.pone.0177737. PubMed PMID: 28545086. PubMed PMCID: PMC5435229.